Experiment-Based Kinematic Validation of Numeric Modeling and Simulated Control of an Untethered Biomimetic Microrobot in Channel

Ahmet Fatih Tabak
Faculty of Engineering and Natural Sciences
Sabanci University
Istanbul, Turkey
tabak@sabanciuniv.edu

Serhat Yesilyurt
Faculty of Engineering and Natural Sciences
Sabanci University
Istanbul, Turkey
syesilyurt@sabanciuniv.edu

Abstract—**Modeling and control of swimming untethered microrobots are important for future therapeutic medical applications. Bio-inspired propulsion methods emerge as realistic substitutes for hydrodynamic thrust generation in micro realm. Accurate modeling, power supply, and propulsion-means directly affect microrobot motility and maneuverability. In this work, motility of bacteria-like untethered helical microrobots in channels is modeled with the resistive force theory coupled with motor dynamics. Results are validated with private experiments conducted on cm-scale prototypes fully submerged in Si-oil filled glass channel. Li-Po battery is utilized as the on-board power supply. Helical tail rotation is triggered by an IR remote control. It is observed that time-averaged velocities calculated by the model agree well with experimental results. Finally, time-dependent performance of a hypothetical model-based position control scheme is simulated with upstream flow as disturbance.**

Keywords- helical wave propagation, mechanical efficiency, model-based control, on-board power supply, resistive force theory, untethered swimming microrobot

I. INTRODUCTION

Progress in micro fabrication techniques and ever-increasing understanding of micro realm [1] lead to promising bio-inspired micro-fluidic and micro-robotic medical applications for therapeutic purposes in particular [2,3,4,5]. Applications such as minimal invasive surgery demand devices like autonomous untethered microrobots.

There are numerous experiments on untethered bio-inspired swimming robots in cm, mm, and μm-scale. Zhang *et al.* [6] presented a magnetically actuated helical filament 30 μm in length, manufactured from GaAs with a soft magnetic nickel attached on one end. Authors demonstrated swimming action controlled by a rotational magnetic field which is subject to the size of the head and strength of the rotating magnetic field driven by Helmholtz coils. Chen *et al.* [7] manufactured a cm-scale untethered bacteria-like robot with four different rigid helical tails driven by four individual dedicated DC-motors. Authors discussed that single-tail actuation is not desirable for control purposes, but three-dimensional gait control is possible with combination of more tails rotating with varied angular velocities. Peyer *et al.* [8] and authors [9] demonstrated the effect of external stimuli such as presence of solid boundaries on the swimming behavior of microrobots with rotating rigid helical tails. Lauga and Powers [10] presented a comprehensive review on methods and elements of swimming in micro dimensions.

Mathematical models are crucial to design and control of microrobots for therapeutic medical applications. Gray and Hancock [11] modeled hydrodynamic forces acting on bacterial flagella based on local resistive force coefficients forming the linear relationship between structural motion, and corresponding fluid resistance for Re < 1, also known as Resistive Force Theory (RFT). Brennen and Winet [12] presented modified coefficient sets for finite-length slender cylinders based on direction and orientation of slender-body motion near flat solid boundaries. Higdon and Muldowney [13] studied the effect of proximity to channel walls on hydrodynamic properties of spherical particles in micro realm extensively by numerical and analytical methods. Lauga *et al.* [14] employed resistance matrix approach coupling 6-dof motion with hydrodynamic force and torque vectors of body and tail of a helical-wave-propagating microrobot moving near solid walls.

Control studies on micro-robotic motility include different approaches. Shechter and Martel [15] carried out experiments controlling position and velocity of bacteria with oxygen gradient in the fluidic medium. Behkam and Sitti [16] discussed the possibility of employing bacteria to move a rather large payload by controlling external stimuli. Mahoney *et al.* [17] experimented on visually assisted velocity control scheme on a magnetically driven helical microrobot with compensation for gravitational attraction. Sakar *et al.* [18] studied direct magnetic positioning of μm-scale payloads in liquid medium by dragging the microrobot to a desired reference position via modifying an external magnetic field.

In this work we conducted experiments with under-actuated two-link untethered bio-inspired robots equipped with on-board power source and rigid helical tails of different geometric configurations. Robots are fully submerged inside a cylindrical glass tube, which is filled with a viscous fluid. Swimming motion is triggered by an IR remote controller and IR receiver circuit embedded in robot body. Rigid helical tail is rotated by a dedicated coreless brushed DC-motor. Displacements of the robots along the channel axis are captured with a CCD-camera.

A time-dependent hydrodynamic model based on RFT including DC-motor dynamics is used to predict the time-

This work was supported in part by the Scientific and Technological Research Council of Turkey under the grant 111M376 (T.A.CF-12-00867).

averaged swimming velocities. Experimental results are used to validate the proposed hydrodynamic model with appropriate calibrations of body resistance coefficients obtained from a single base-design. Numerical and experimental data for time-averaged forward velocity are found to agree reasonably well. Additionally, we studied hydrodynamic efficiency of the robot with modified wave geometry.

Lastly, we implemented a model-based position control scheme based on PI-control and simulated its time-dependent performance for a particular position reference with a time-dependent upstream velocity for disturbance.

II. METHODOLOGY

A. *Biomimetic Robot and Experimental Setup*

Biomimetic robot is comprised of a payload, i.e. body, and a right-handed helix shaped rigid tail attached with a revolute joint as demonstrated in Fig. 1. The design presented here is a successor to the prototype used earlier by Erman and Yesilyurt [19]. Geometric properties of the components are presented in Table I.

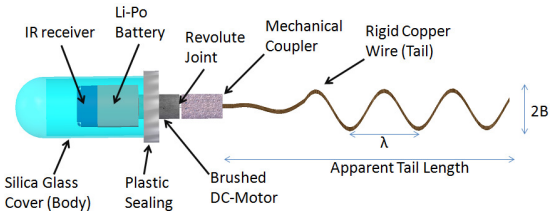

Figure 1. Untethered biomimetic robot structure.

Helix shaped tail is manufactured by winding and deforming a copper wire, which is 1 mm in diameter. Apparent tail length, i.e. length of the helix, is set to 60 mm regardless of wave length and wave amplitude. One end of the rigid tail, which is inserted into the mechanical coupler, is deformed with a steep hyperbolic tangent profile. Mechanical coupler holds the rotor of DC-motor on the other side (Fig. 1).

Body assembly is sealed by a cylindrical transparent silica-glass with one end closed as a smooth spherical surface, and with a plastic sealing on the other end. Plastic sealing is also constitutes the housing for brushed DC-motor simulating the bacterial motor; however, is not analogous to it [20]. Power leads of the DC-motor are secured within the body and connected to the driving circuitry composed of IR receiver and single-cell 3.7 V 70 mA·h rechargeable Li-Po battery, whereas motor shaft, i.e. end of the rotor, is outside and inserted into mechanical coupler forming the revolute joint (Fig. 1).

TABLE I. GEOMETRIC PROPERTIES OF BODY

Overall Body Length / Diameter	35 mm / 18 mm
Total Body Mass	10.7 g
Li-Po Battery Dimensions	5.5 mm x14mm x17mm
Coreless Brushed DC-Motor Diameter	6 mm
Mechanical Coupler Diameter / Length	6 mm / 10 mm
Mechanical Coupler Mass	0.8 g

Untethered biomimetic robot is fully submerged and placed inside a constant cross section glass tube with both ends open sitting in a Si-oil filled tank as shown in Fig. 2. Glass tube has an inner radius of 20 mm, and is 350 mm in length. It is noted that long axis of the tube is also the **X**-axis in lab frame. Physical properties of the Si-oil are temperature-independent and measured as $\rho = 985$ kg/m^3 and $\mu = 3.5$ Pa·s.

Tail rotation is triggered by an external IR remote controller, and swimming motion inside the glass tube is captured by a CCD-camera sampling at 30 fps for at least 5 complete periods of body rotation with respect to lab frame, which is inherently slower than tail rotation. Plastic sealing on the body is symmetrically coded with different colored stripes in order to determine the body rotation rate (see Fig. 3).

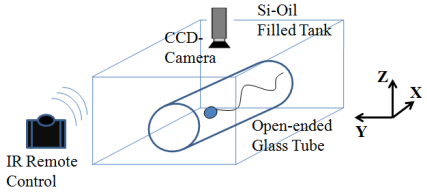

Figure 2. Experimental Setup: Si-oil filled tank, glass tube, CCD-camera, untethered biomimetic robot.

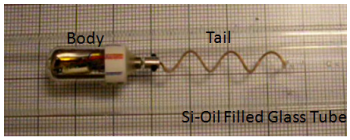

Figure 3. Untethered biomimetic robot submerged in Si-oil inside glass tube.

B. *Mathematical Model*

Resistive force theory [11] and scallop theorem [21] lead to omission of all inertial terms leading to a first order system. Furthermore, presence of a revolute joint and using rotational freedom of the tail as the means of propulsion result in 6-dof rigid-body motion to solve for. In effect, thrust obtained by rotating rigid tail, resultant counter body rotation with DC-motor dynamics and the fluid drag due to rigid-body translation of the entire untethered robot are incorporated in the equation of motion as follows:

$$\begin{aligned} \mathbf{F}_d + \mathbf{F}_p &= \mathbf{0} \\ \mathbf{T}_d + \mathbf{T}_p + \mathbf{T}_f &= \mathbf{0} \end{aligned} \tag{1}$$

where the subscripts *d*, *p,* and *f* denote drag, propulsion, and effective friction respectively. It is noted that equation of motion is written in the swimmer frame with respect to its center of mass (see Fig. 4).

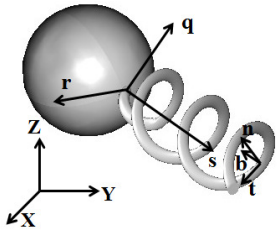

Figure 4. Frames of reference: lab frame (**XYZ**); swimmer frame (**sqr**); local Frenet-Serret frames (**tnb**) on right-handed helix tail.

Propulsion force and torques in (1) are obtained with a linear relationship given by:

$$\begin{bmatrix} \mathbf{F}_p \\ \mathbf{T}_p \end{bmatrix} = \mathbf{M} \begin{bmatrix} \mathbf{0} \\ \boldsymbol{\Omega}_t \end{bmatrix} \tag{2}$$

where ‘$\mathbf{\Omega}_t$’ is the vector containing solely **s**-axis rotation of the tail, i.e. $\mathbf{\Omega}_t = \begin{bmatrix}\omega_{\mathbf{s}} & 0 & 0\end{bmatrix}'$ where ‘ ' ’ stands for transpose action. ‘**M**’ is a 6-by-6 resistance matrix of the rigid tail and modeled as:

$$\mathbf{M} = \int_0^L \begin{bmatrix} \mathbf{RCR}' & -\mathbf{RCR}'\mathbf{S} \\ \mathbf{SRCR}' & -\mathbf{SRCR}'\mathbf{S} \end{bmatrix} \mathrm{d}s \tag{3}$$

where ‘**R**’ is the rotation between local Frenet-Serret frames [22] on numerically discretized tail, ‘**C**’ is the diagonal local resistance matrix based on resistive force theory [11], ‘**S**’ is the skew symmetric matrix for local cross products, and ‘*L*’ is the actual length of the wire. Local resistance matrix in (3) contains the following resistive force coefficients of choice given by [12]:

$$c_t = \begin{cases} -\dfrac{2\pi\mu}{\ln(\lambda/d) - 0.807 - 3\lambda/16h} & , \dfrac{\lambda}{2h} \le 1 \\ -\dfrac{2\pi\mu}{\ln(2h/d)} & , \dfrac{\lambda}{2h} > 1 \end{cases}$$

$$c_n = c_b = \begin{cases} -\dfrac{4\pi\mu}{\ln(\lambda/d) + 0.193 - 3\lambda/8h} & , \dfrac{\lambda}{2h} \le 1 \\ -\dfrac{4\pi\mu}{\ln(2h/d)} & , \dfrac{\lambda}{2h} > 1 \end{cases} \tag{4}$$

where ‘h’ is the local distance of the center line of the wire to the nearest point on the channel surface, ‘d’ is the wire radius, and ‘λ’ is the helical wave length. Local distance is dependent on **s**-position, wave amplitude ‘B’, and position of the swimmer with respect to channel boundaries.

Drag force and torque vectors in (1) are obtained in a similar fashion:

$$\begin{bmatrix} \mathbf{F}_d \\ \mathbf{T}_d \end{bmatrix} = (\mathbf{M}^* + \mathbf{N}) \begin{bmatrix} \mathbf{U} - \mathbf{W} \\ \mathbf{\Omega} \end{bmatrix} \tag{5}$$

where ‘**U**’ and ‘$\mathbf{\Omega}$’ denote rigid-body translation and rotation vectors of the untethered biomimetic robot respectively. ‘**W**’ is upstream velocity vector. In (5), ‘$\mathbf{M}^*$’ is the reduced resistance matrix of the swimmer tail, i.e. the row and the column elements of ‘**M**’ related to non-zero element of ‘$\mathbf{\Omega}_t$’ are reduced to zero due to the fact that resultant **s**-rotation will be of body due to implicit conservation of angular momentum. The body resistance matrix ‘**N**’ is specified akin to (3) [23].

Effective friction torque in (1) is obtained by means of coupled mechanical and electrical properties of the actuation system (see Fig. 5). All electromechanical properties except rotor friction are experimentally measured and presented in Table II: effective battery voltage ‘V’ and total electrical resistance ‘R’ are dependent on motor current ‘I’.

Motor current ‘I’ is determined by the following differential equation:

$$\mathrm{L}\frac{\mathrm{dI}(t)}{\mathrm{d}t} + \mathrm{R}(t)\mathrm{I}(t) = \mathrm{V}(t) - \mathrm{K_b}\omega_{eff} \tag{6}$$

where ‘L’ is the motor inductance, ‘ω_{eff}’ is the total instantaneous rotational velocity of the rotor, and ‘$\mathrm{K_b}$’ is the back-emf constant of the DC-motor [24]. Linear relation constant ‘B_{eff}’ between effective rotational friction, which is dominated by the interaction between swimmer body and channel wall, and the instantaneous rotational velocity of the motor is computed online by the following equation [24]:

$$(\mathrm{B}_{eff} + \mathrm{K_b}\mathrm{K_m}/\mathrm{R}(t))\omega_{eff} = \mathrm{V}(t)\mathrm{K_m}/\mathrm{R}(t) - T_{\mathbf{s}} \tag{7}$$

where ‘$\mathrm{K_m}$’ is the torque constant, and ‘$T_{\mathbf{s}}$’ is the instantaneous hydrodynamic load on the rotor. It is noted that moments of inertia of swimmer or motor are not included. Once ‘B_{eff}’ is resolved, the friction torque in (1) is given by:

$$\mathbf{T}_f = \begin{bmatrix} -\mathrm{B}_{eff}\omega_{eff} & 0 & 0 \end{bmatrix}' \tag{8}$$

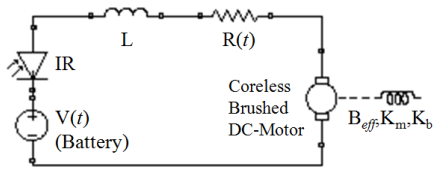

Figure 5. Electromechanical representation of actuation system.

TABLE II. MEASURED MOTOR AND BATTERY PROPERTIES

R(*t*)	10.4 + 30 exp(– 54.6 I(*t*)) + exp(I(*t*)) – 1.555 I(*t*) Ohm
V(*t*)	3.7 – 0.8 I(*t*) V
L	0.082 H
$\mathrm{K_m}$	0.00045 N·m/A
$\mathrm{K_b}$	0.004 V·s/rad

Hydrodynamic efficiency of the untethered biomimetic robot is defined as the ratio of motor power rotating the rigid tail with observed ‘$\omega_{\mathbf{s}}$’ to useful hydrodynamic work utilized for net forward motion:

$$\eta = \frac{\mathrm{U}_{\mathbf{s}}^2(\mathbf{N}_{11} + \mathbf{M}_{11})}{T_{\mathbf{s}}\omega_{\mathbf{s}}} \tag{9}$$

where ‘$\mathbf{N}_{11}$’ and ‘$\mathbf{M}_{11}$’ are the first diagonal elements of body and tail resistance matrices respectively, which correspond to translational forward velocity. Electrical efficiency is not included in the analysis due to the fact that heat generation inside the DC-motor is not measured during experiments.

C. PI-Control

PI-control is implemented in order to simulate the behavior of untethered biomimetic robot model under uniform upstream velocity condition as specified in (10) with initial and time-dependent components acting as disturbance (see Fig. 6).

$$W_{\mathbf{X}} = W_0 + W \begin{cases} 0 \Leftarrow t < t_0 \;\&\; t > t_1 \\ 1 \Leftarrow t_1 \ge t \ge t_0 \end{cases} \tag{10}$$

where ‘t_0’ and ‘t_1’ are the instances for rising edge and falling edge upstream conditions respectively. Control output is actually embedded in local rotation matrix ‘**R**’ due to helical wave propagation on tail (see (3)) and implemented as:

$$\omega_{\mathbf{s}} = \mathrm{K_p}e + \mathrm{K_i} \begin{cases} \int e \,\mathrm{d}t & \Leftarrow \mathrm{I}(t) < \alpha \mathrm{I_{lim}} \\ 0 & \Leftarrow \mathrm{I}(t) \ge \alpha \mathrm{I_{lim}} \end{cases} \tag{11}$$

where ‘e’ is the position error, ‘$\mathrm{K_p}$’ is the proportional gain, ‘$\mathrm{K_i}$’ is the integrator gain, ‘$\mathrm{I_{lim}}$’ is the maximum possible current without destroying the circuit shown in Fig. 5, and ‘α’

is a safety factor, e.g. 0.99. Additionally, a rudimentary anti-windup method is implemented in order to prevent numerical overflow due to integrator gain: as the motor current is saturated or position error goes to zero, negative of recent error integration in (11) is sent back to the ODE solver resetting the entire integral back to its initial value, i.e. zero. Derivative gain is excluded in order to avoid introducing additional numerical stiffness to the model.

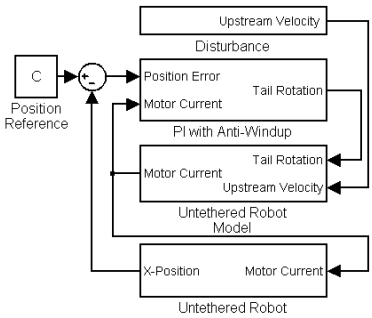

Figure 6. Model-based PI-control scheme.

III. RESULTS

A. *Experiment-Based Model Verification*

Images captured by CCD-camera are inspected frame-by-frame in order to resolve the body rotation rate ' Ω_s ', tail rotation rate ' ω_s ', and swimmer's forward velocity ' U_s '. Results are obtained by averaging out five distinct measurements and error bars are calculated with 95 per cent confidence interval. Then, observed tail rotation rates are employed in simulations as actuation frequencies. Motor current 'I' and hydrodynamic efficiency ' η ' values are calculated by the proposed model.

Equation of motion given by (1) and motor current (6) are solved by Adams-Bashforth-Moulton PECE solver [25] for three complete periods on a 64-bit Xeon machine running on Linux. Each simulation took approximately two to three seconds to complete at least three complete periods and time-averaged results presented in this text are obtained via averaging out the final two periods.

There are sixteen rigid tails with combinations of four different amplitude and four different wave lengths (see Fig. 7-8), and only one body to assemble with. Although assembled robots have 6-dof motion capability, due to inadequate buoyancy force combined with the effect of the glass channel, overall swimming action is effectively dominated by **X**-axis translation with negligible lateral motion, i.e. hovering above the glass tube surface. As a result, long axis of the channel and **s**-axis of the swimmer typically remained parallel to each other during experiments. Consequently, we mainly focused on translational **s**-velocity, which is in effect identical to **X**-velocity, and body rotation rates along with motor currents and efficiency levels obtained by (1), (6) and (9).

In order to compensate for the channel effect and proximity to the channel walls in simulations, drag coefficients of the body are calibrated with respect to the base-case model (see Fig 7c and 7g) for only once: translational **s**-drag coefficient is multiplied by 2.5 and rotational **s**-drag coefficient is multiplied by 0.2. This particular correction set is used for all sixteen body-tail assemblies rather than determining sixteen individual correction sets. It is noted that Re ≈ 0.005 is calculated for the base-case.

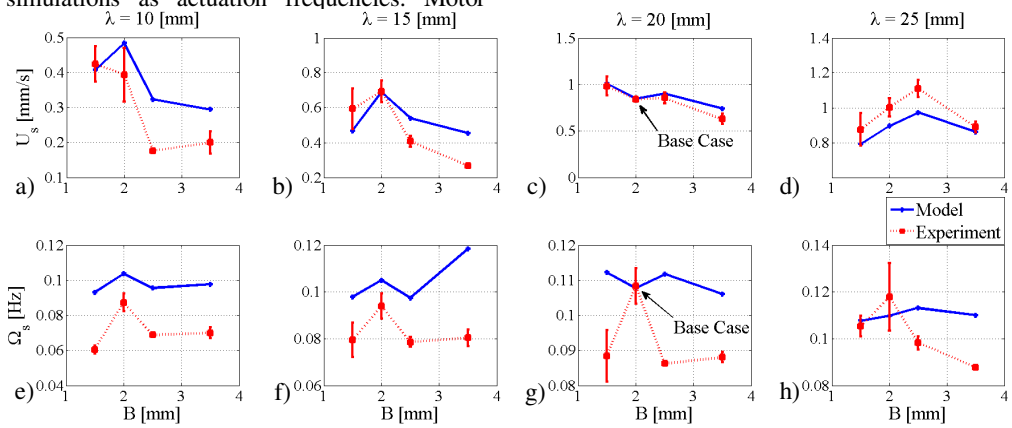

Figure 7. Forward lab velocity with error bars (a-d) and rotor actuation frequency with error bars (e-h) of untethered biomimetic robot.

In Fig. 7a-d, time-averaged **s**-velocity values, in other words the **X**-velocity down the channel's long axis, obtained by simulations are compared with experimental results. It is observed that forward velocity increases as the wave length increases. Amplitude dependency shows an erratic behavior in both numerical and experimental results; but has a clear adverse effect in Fig 7a-c. In general, the sensitivity of forward swimming action to wave length and wave amplitude is well predicted.

In Fig. 7e-h, averaged out body **s**-rotation rates ' Ω_s ' obtained by experiments and simulations are presented. It is observed that change in wave length has no considerable effect on rotation rates but a minute fluctuation. However, change in wave amplitude has an irregular effect on body rotation rates in both simulation and experimental results. Although numerical results show error levels up to fifty per cent with experimental results, numerical values are reasonably close to each other.

Mechanical efficiency, motor current, and total rotation rates of the untethered biomimetic robots are presented in Fig. 8. Efficiency values (see Fig. 8a-d) are at most on the order of one due to severe viscous losses by means of heat output, which is fully anticipated [26]. Results demonstrate that small wave lengths with a fixed apparent tail length is not desirable since efficiency levels drop further as depicted in Fig. 8a. On

the other hand, further increase in wave length does not affect efficiency values. It is also observed that increasing wave amplitude results in increasing efficiency levels with all wave lengths presented in this text.

It is shown in Fig. 8e-h that the motor current increases with decreasing wave length and increasing wave amplitude which is consistent with decreasing effective rotation rate of the DC-motor 'ω_{eff}' as demonstrated in Fig. 8i-l. Decrease in rotation rate leads to increasing current because of decreasing back-emf effect in (6) with right hand side numerically surpassing the left hand side in (7).

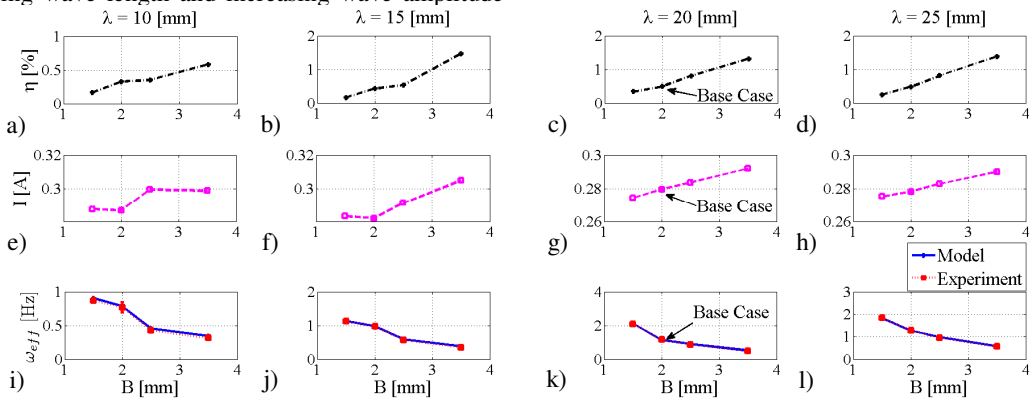

Figure 8. Computed mechanical efficiencies (a-d), motor currents (e-h), and rotor rotation rates (i-l) of untethered biomimetic robot.

B. *Simulated Control Performance*

The following scenario is studied in order to demonstrate the behavior of the model and PI-control algorithm as a model-based control scheme to predict required motor current with saturation as required. The base-case combination presented in Fig. 7-8 is employed with limit current of 500 mA, and final destination of -27 mm down the channel's long axis from starting position of X = 0 mm. Upstream velocity is designated as W_0 = 0 mm/s and W= 25 mm/s; on the opposite direction of observed swimming velocity down the long axis of the channel, and with the rising edge occurring at t = 4 s and falling edge ensuing at t = 8 s.

In Fig. 9-11 it is demonstrated that in all three cases motor current climbs up to 300 mA immediately and saturates at 500 mA when proportional gain K_p is set to 12 for given position error, and drops to zero as position error goes to zero. However, proportional control renders inadequate output to follow the reference while untethered biomimetic robot is under the influence of upstream flow because of the current saturation (see Fig. 10). Consistent with experimental results, motor current is well above zero unless position error drops to zero which is in part subject to numerical error.

As the proportional gain is reduced below K_p = 12, convergence of the system decreases and motor current falls below the maximum limit (see Fig. 10) down to 300 mA and drops to zero simultaneously with diminishing position error. Then, integral gain is set to K_i = 12 with K_p = 10 in order to overcome the effect of upstream velocity with a fast convergence rate which results in 4 mm overshoot around t = 0.9 s that dissipates gradually (see Fig. 9). However, corresponding current demand does not dissipate as fast due to integration history and first order nature of the model (see Fig. 10). Typically, higher integrator gain causes higher overshoot but offer a better performance in managing upstream conditions as demonstrated in Fig. 9.

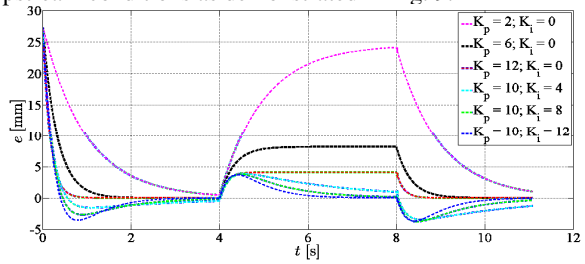

Figure 9. Calculated position error under different PI-configurations.

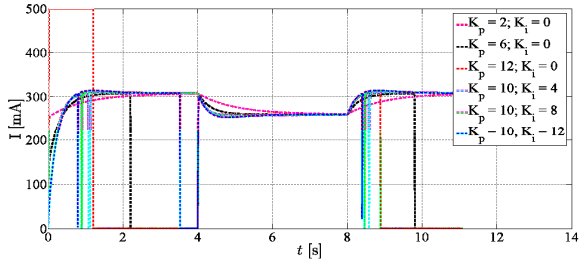

Figure 10. Predicted motor current under different PI-configurations.

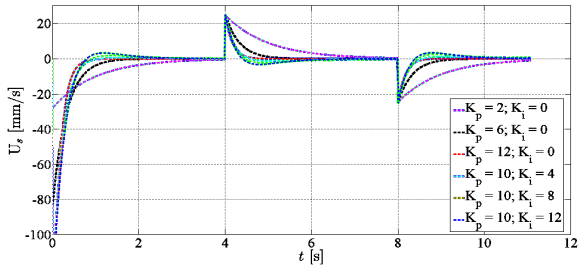

Figure 11. Calculated instantaneous **X**-velocities of base-case untethered biomimetic robot under different PI-configurations.

Predicted robot velocity in Fig. 11 is consistent with position error and motor current plots. It is observed that simulated instantaneous velocity of the untethered

biomimetic robot may reach up to velocities on the order of 100 mm/s.

IV. Conclusion

We conducted experiments with untethered biomimetic robots swimming in channels while carrying on-board power source. Sixteen rigid helical tails comprising combinations of four different wave amplitudes and four different wave lengths are used. Glass channel with untethered bio-inspired robot inside is fully submerged in Si-oil bath in order to satisfy Re < 1, and channel ends were open to the Si-oil reservoir at all times. Swimming action is triggered by an on-off mode IR remote controller. Actuation frequency of each body-tail assembly is dependent on the overall swimmer-geometry and recorded along with forward velocities and body rotation rates in lab frame.

Observed tail rotation rates in lab frame are used as actuation frequencies to predict the 2-dof motion and motor-current of the untethered biomimetic robot via proposed RFT model combined with DC-motor dynamics. Lateral motion is omitted in RFT model since robot is only able to hover above the channel surface due to its weight. Surface effects attributed to fluid drag on the body are calibrated for only once with respect to a selected base-case assembly. Furthermore, an effective rotational friction torque constant is incorporated into equation of motion obtained by first-order DC-motor equations. It is observed that predicted forward velocity and body rotation rates are in well agreement with each other. However, body rotation rates are found to be partially out of sync due to geometric irregularities of swimmer's body and mechanical coupler.

We defined a hydrodynamic efficiency based on useful mechanical power transfer by means of ratio of the work done by forward shear on towed body to the work done by the rotating tail against effective hydrodynamic load on DC-motor. Efficiency values are found to be on the order of 0.1 to 1 per cent.

Finally, we implemented a PI-control algorithm to simulate the performance of the RFT model on the under-actuated biomimetic robot motility with a hypothetical model-based control scheme. Proportional gain is established adequate for position control purposes due to first order nature of the RFT model, however, it is demonstrated that integrator gain with anti-windup is necessary in order to determine the required 'ω_{eff}' and to drive maximum possible current to minimize position error under the influence of time-dependent upstream velocities acting as disturbance. It is noted that gravitational pull has a stabilizing effect on the studied untethered robot motility.

Acknowledgments

The authors wish to thank Prof. Ahmet Onat at Sabanci University for his invaluable comments.

References

[1] K. D. Wise, "Integrated Sensors, MEMS, and Microsystems: Reflections on a Fantastic Voyage," *Sensors and Actuators*, Serie A, Vol. 136, pp. 39-50, 2007.

[2] J. Edd, S. Payen, B. Rubinsky, M. L. Stoller, and M. Sitti, "Biomimetic Propulsion for a Swimming Surgical Micro-Robot," *IEEE/RSJ Intelligent Robotics and Systems Conference* (*IROS*), Vol. 3, pp. 2583-2588, Las Vegas, USA, October 2003.

[3] S. Martel, "Collective Methods of Propulsion and Steering for Untethered Microscale Nanorobots Navigating in the Human Vascular Network," *Journal of Mech. Eng. Science*, pp. 1505-1513, 2010.

[4] B. J. Nelson, I. K. Kaliakatsos, and J. J. Abbott, "Microrobots for Minimally Invasive Medicine," *Annu. Rev. Biomed. Eng.,* Vol. 12, pp. 55-85, April, 2010.

[5] R. Bogue, "The Development of Medical Microrobots: A Review of Progress," *Industrial Robot: An International Journal*, Vol. 35, No. 4, pp. 294-299, 2008.

[6] L. Zhang, J. J. Abbott, L. Dong, B. E. Kratochvil, D. Bell, and B. J. Nelson, "Artificial Bacterial Flagella: Fabrication and Magnetic Control," *Applied Physics Letters*, Vol. 94, pp. 064107-1-3, February, 2009.

[7] B. Chen, S. Jiang, Y. Liu, P. Yang, S. Chen, "Research on the Kinematic Properties of a Sperm-Like Swimming Micro Robot," *Journal of Bionic Engineering*, Vol. 7, Suppl., pp. S123-S129, 2010.

[8] K. E. Peyer, L. Zhang, B. E. Kratochvil, B. J. Nelson, "Non-Ideal Swimming of Artificial Bacterial Flagella Near a Surface," *IEEE International Conference on Robotics and Automation*, Anchorage, Alaska, May 2010.

[9] A. F. Tabak, F. Z. Temel, S. Yesilyurt, "Comparison on Experimental and Numerical Results for Helical Swimmers inside Channels," *IEEE/RSJ Intelligent Robotics and Systems Conference* (*IROS*), San Frascisco, USA, June 2011.

[10] E. Lauga, T. R. Powers, "The Hydrodynamics of Swimming Microorganisms," *Rep. Prog. Phys*., Vol. 72, 096601, 2009.

[11] J. Gray, G. J. Hancock, "The Propulsion of Sea-Urchin Spermatozoa," *J. Exp. Biol.*, Vol. 32, pp. 802-814, 1955.

[12] C. Brennen, H. Winet, "Fluid Mechanics of Propulsion by Cilia and Flagella," *Ann. Rev. Fluid Mech.*, Vol. 9, pp. 339-398, 1977.

[13] J. J. L. Higdon, G. P. Muldowney, "Resistance Functions for Spherical Particles, Droplets and Bubbles in Cylindrical Tubes," *J. Fluid Mech*. Vol. 298, pp. 193-210, 1995.

[14] E. Lauga, W. R. DiLuzio, G. M. Whitesides, H. A. Stone, "Swimming in Circles: Motion of Bacteria Near Solid Boundaries," *Biophysical Journal*, Vol. 90, pp. 400-412, 2006.

[15] E. Shechter, S. Martel, "Principle of Motion Control of Bacterial Micro-Robots Using Oxygen Gradients," *IEEE/ASME International Conference of Advanced Intelligent Mechatronics*, Montreal, Canada, July 2010.

[16] B. Behkam, M. Sitti, "Towards Hybrid Swimming Microrobots: Bacteria Assisted Propulsion of Polystyrene Beads," *EMBS'06 28th Annual International Conference of the IEEE*, Aug 2006.

[17] A. W. Mahoney, J. C. Sarrazin, E. Bamberg, J. J. Abbott, "Velocity Control with Gravity Compensation for Magnetic Helical Microswimmers," *Advanced Robotics*, Vol. 25, pp. 1007-1028, 2011.

[18] M. S. Sakar, E. B. Steager, D. H. Kim, A. A. Julius, MJ. Kim, V. Kumar, H. J. Pappas, "Modelling, Control and Experimental Charactrerization of Microrobots," *The International Journal of Robotic Research*, Vol. 30, No. 6, pp. 647-658, 2011.

[19] A. G. Erman, S. Yesilyurt, "Swimming of Onboard-Powered Autonomous Robots in Viscous Fluid Filled Channels," *IEEE International Conference on Mechatronics (ICM)*, Istanbul, Turkey, April 2011.

[20] H. C. Berg, "The Rotary Motor of Bacterial Flagella," *Annu. Rev. Biochem.*, Vol. 72, pp. 19-54, 2003.

[21] E. Lauga, "Life Around the Scallop Theorem," *Soft Matter.*, Vol. 72, pp. 19-54, 2010.

[22] A. J. Hanson, H. Ma, "Visualizing Flow with Quaternion Frames," in *Proc. of the conference on Visualization '94*, Washington, D.C., 1994, pp. 108-115.

[23] J. Happel, H. Brenner, *Low Reynolds Number Hydrodynamics*, N.J.: Prentice-Hall, Inc., 1965.

[24] M. W. Spong, M. Vidyasagar, *Robot Dynamics and Control*, USA: John Wiley & Sons, 1989.

[25] L. F. Shampire, M. K. *Gordon, Computer Solution of Ordinary Differential Equations: The Initial Value Problem*, USA:Oxford University Press, 1985.

[26] E. M. Purcell, "Life at Low Reynolds Number," *American Journal of Physics*, Vol. 45, No. 1, pp. 3-11, 1977.